How to cite: *Angew. Chem. Int. Ed.* **2022,** *61,* e202214244
International Edition: doi.org/10.1002/anie.202214244
German Edition: doi.org/10.1002/ange.202214244

Zn-Ion Batteries

Organic Zinc-Ion Battery: Planar, π-Conjugated Quinone-Based Polymer Endows Ultrafast Ion Diffusion Kinetics

*Fei Ye, Qiang Liu, Hongliang Dong, Kailin Guan, Zhaoyang Chen, Na Ju, and Linfeng Hu**

Abstract: A novel poly(phenazine-alt-pyromellitic anhydride) (PPPA) has been successfully designed and synthesized via a condensation polymerization strategy as promising cathode material in organic zinc-ion batteries. Electrochemical quartz crystal microbalance (EQCM), FTIR and XPS characterizations verify a reversible Zn^{2+}-coordination mechanism in our PPPA cathode. Intriguingly, an ultrahigh Zn^{2+} diffusion coefficient of 1.2×10^{-7} cm^2s^{-1} was found in this large π-conjugated system, which is the highest one among all organic cathode materials for zinc-ion batteries. Theoretical calculations reveal the extended π-conjugated plane in our PPPA sample results in a significant reduction on energy gap, effectively accelerating intramolecular electron transfer during charge/discharge process. Our finding provides insights to achieve high zinc-ion transport kinetics by a design strategy on planar polymer system.

Introduction

Aqueous batteries have attracting considerable interests with the increasingly serious safety issues of commercial lithium-ion batteries based on flammable organic electrolytes.[1] Among them, aqueous zinc-ion batteries (AZIBs) have been regarded as the most appealing next-generation energy storage devices owing to its prominent merits on the low redox potential, high theoretical capacity, excellent water compatibility and relatively low cost.[2] Since most of AZIBs use metallic Zn foil as the anode, the cathode materials play a critical role in the overall battery performance. During the past few years, great progress has been made to demonstrate number of novel cathode materials including inorganic Mn, V, Mo-based oxides/sulfides, and metal-organic compounds of Prussian blue analogous (PBAs).[3] Nevertheless, these inorganic lattices or metal-organic frameworks generally suffer from structural collapse due to the remarkable change on crystal structure and volume during charging and discharging process, giving rise to severe capacity fading and poor long-term lifespan.[4]

The most recent progress on the discovery of Zn^{2+} storage in some organic quinone compounds sheds light on well addressing of this problem.[5] Compared to inorganic or PBAs cathodes, organic electrode materials are more flexible at accommodating guest ions. Typically, small-molecule quinones including calix [4] quinone (C4Q),[6] tetraamino-p-benzoquinone (TABQ),[7] 9,10-phenanthraquinone (PQ),[8] etc., exhibit a reversible capability of capturing Zn^{2+} by coordination mechanism from highly reversible ionization of C=O bonds, in which the flexible structure could provide elastic matrixes for Zn^{2+} storage to avoid the occurrence of lattice expansion/shrinkage and structural strain compared to the inorganic cathodes. Unfortunately, most of these quinone compounds are prone to dissolve in the electrolyte during the charging/discharging process, also resulting in the severe capacity fading and deterioration of the cycling lifespan.[9]

Polymerization from quinone monomers has been developed as an effective strategy to eliminate the dissolution phenomenon in electrolyte. For example, Chen and co-workers synthesized quinone-based polymer with superior chemical stability by linking quinone-derived monomers via thioether linkage.[10] Tang et al. proposed the grafting quinone molecules onto polymer backbones could be another feasible approach to achieve stable Zn^{2+}-hosting material.[11] Although these polymers are highly attractive for the potential application on aqueous zinc-ion storage, their electrochemical performance on capacity, rate capability, and cyclability is still far from satisfaction. One of the main reasons should be due to the sluggish Zn^{2+} diffusion in this polymer consisted of twisted molecule chains with rather poor molecular planarity.[4a,11] Making a breakthrough on Zn^{2+} diffusion kinetics in quinone-based polymer to overcome its performance bottleneck is of great importance, but it is still highly challenging.

Noted that expansive molecular plane achieved by extended the π-conjugated structure can provide abundant open two-dimensional channels for fast zinc-ion transport. More importantly, the dense π-conjugated stacking results in abundant delocalized π-electrons, which are favorable for facilitating ions diffusion during the electrochemical redox reactions.[12] This inspires us to consider whether one can directly synthesize linear quinone polymers with planar structure. Inspired by this consideration, herein, we designed a linear π-conjugated quinone-based polymers, namely poly-(phenazine-alt-pyromellitic anhydride) (PPPA), via a one-step polycondensation reaction with the electroactive mono-

[*] Dr. F. Ye, Q. Liu, K. Guan, Z. Chen, N. Ju, Prof. L. Hu
School of Materials Science and Engineering,
Southeast University, Nanjing, 211189 (China)
E-mail: linfenghu@seu.edu.cn
Dr. H. Dong
Center for High Pressure Science and Technology Advanced Research, Shanghai, 201203 (P. R. China)

mers of phenazine and pyromellitic anhydride (PMDA). Utilizing the cathode material for AZIBs, it delivers a discharge capacity of 210.2 mAh g^{-1} at 50 mA g^{-1} and an excellent cycling stability over 20000 cycles at 5000 mA g^{-1}. More impressively, an ultrahigh Zn^{2+} diffusion coefficient of 1.2×10^{-7} $cm^2 s^{-1}$ has been achieved, which is several orders of magnitude higher than those of conventional cathode materials, and also the highest one in all of the organic compounds up to date. Our work provides the insights on the achievement of ultrahigh Zn^{2+} transport kinetics through the rational design of planar π-conjugated structure in novel quinone-based polymer.

Results and Discussion

The synthetic route of PPPA material is schematically illustrated in Scheme 1a. Firstly, the mixture of $AlCl_3$ and NaCl (a molar ratio of 2:1) was heated at 160 °C to produce a liquid fused salt. Secondly, phenazine and PMDA powder was introduced into the fused salt and then heated at 250 °C with continuously stirring for 24 h, and then the black PPPA powder sample (inset in Figure 1a) with a yield of approximate 72 % was successfully obtained. The PPPA was formed by the Friedel–Crafts reaction mechanism of phenazine with pyromellitic anhydride as shown in Scheme 1b. Briefly, the anhydride was firstly catalyzed by $AlCl_3$ to form the acyl with positive charges. Then, the electrophilic substitution occurred between the acyls and electron-rich aromatic rings in phenazine, resulting in the aromatic ketone structures. Finally, PPPA polymer was produced by repeating the above steps. Moreover, there is no rearrangement of carbon atoms during the reaction process due to the high stability through resonance effect. Meanwhile, the passivation of aromatic rings via the introduction of acyl can inhibit the generation of multi-substituted by-products.

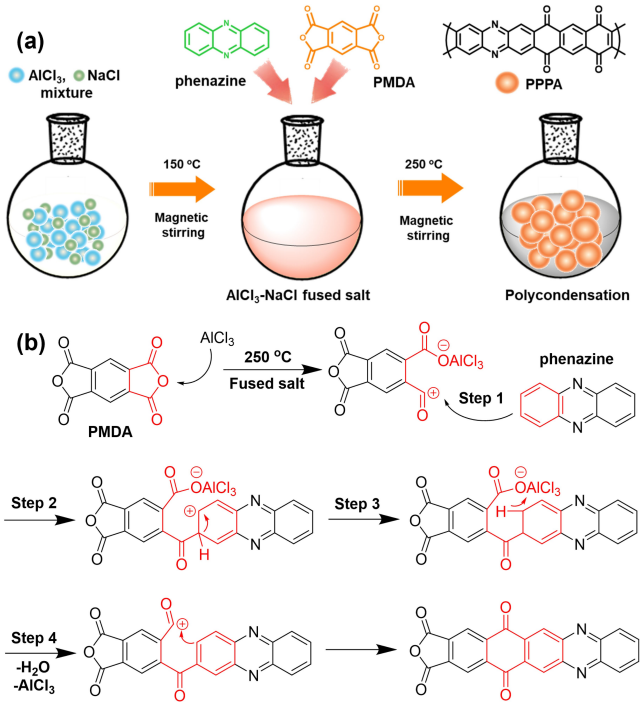

Scheme 1. a) The synthetic procedure and b) Friedel–Crafts reaction mechanism.

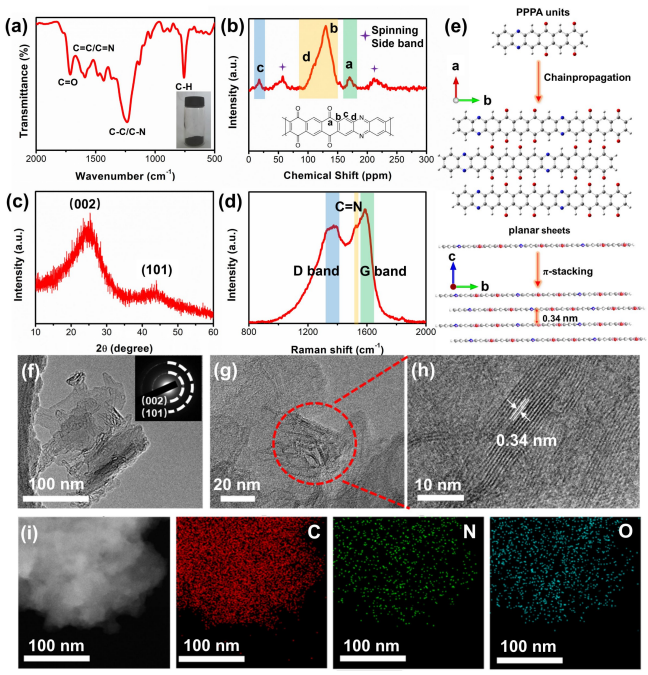

Figure 1. a) FTIR spectra. b) ^{13}C solid-state NMR spectra. c) XRD pattern. d) Raman spectroscopy. e) Schematic illustration on the dynamic π-π stacking process to form planar PPPA. f–h) TEM and HRTEM images. Inset in (e) is the corresponding SAED pattern. i) EDS mapping of C, N and O.

The detailed structure of our PPPA sample was then characterized by Fourier transform infrared (FTIR), nuclear magnetic resonance (NMR), X-ray diffraction (XRD), Raman and transmission electron microscopy (TEM) measurements. The characteristic peak at 1710 cm^{-1} in the FTIR spectroscopy is attributed to the stretching vibrations of C=O bond.[13] The skeletal vibration of aromatic rings (the C=C or C=N bond) could be affirmed by the characteristic peaks within 1540–1640 cm^{-1}, while the peaks around 1200–1300 cm^{-1} were ascribed to the stretching vibration of the C–C or C–N bonds.[14] ^{13}C solid-state NMR characterization was carried out to further confirm the structural information. As shown in Figure 1b, the fingerprint peaks at 17, 110, 130 and 170 ppm identify the existence of four distinct types of C atoms (e.g., C–H, C=N, C=O, and C=C) as marked in the molecule structure inserted in Figure 1b.[15] In particular, the overlapped peaks in the range from 100 to 150 ppm could be due to the rigid π-conjugated molecular structure, resulting in the widening of the NMR characteristic peaks. Furthermore, the chemical composition respectively obtained from elemental analysis and theoretical molecular formula are listed in Table S1. The slight deviation between theoretical and the experimental value suggests the successful synthesis to achieve the fused-ring compound integrating quinone and phenazine.

Powder XRD pattern in Figure 1c exhibits noticeable peak broadening, implying its low crystallinity. Note that the peak at around 25° corresponding to a d-spacing of 0.35 nm well matches the (002) lattice planes of graphite structures.[16] Raman spectra in Figure 1d further confirm this graphitized structure. The characteristic peak at 1520 cm^{-1} representing the C–N bond. The peaks located at about 1358 and 1598 cm^{-1} could be respectively assigned to the D and G band. Considering the relatively higher intensity of G band than D band, the in-plane structure of PPPA can be understood by an analogous graphene configuration.[4a] The delocalized aromatic structural units were converted into planar aromatic sheets in the polymerization process, and then these layers stack together by π-π stacking interactions to become graphite-like morphologies (Figure 1e).[16] The dynamic morphology evolution during the polymerization process was identified by SEM observation in Figure S1. The as-grown sample at different polymerization time of 2, 12, 24 h displays analogous particle morphology with irregular shape. The particle size increases gradually with prolonging the polymerization time until 24 h. The sample synthesized at this time shows rather smooth surface with a specific surface area of 100 $m^2 g^{-1}$ evaluated by the Brunauer–Emmett–Teller method (Figure S2). TEM image in Figure 1f reveals a two-dimensional morphology consisted of ultrathin, semitransparent nanosheets. The corresponding selected area electron diffraction (SAED) pattern exhibits polycrystalline diffraction rings, further confirming the crystallinity of our PPPA sample. In addition, lattice fringes with an interlayer spacing of 0.34 nm was clearly observed at the edge of the sheets in the high-resolution transmission electron microscopy (HRTEM) images (Figure 1h), which is well in agreement with the d-spacing of 0.35 nm in the XRD pattern. The corresponding EDS mapping results (Figure 1i) confirm homogeneous distribution of C, N and O species in the polymer.

The zinc-ion storage performance was then evaluated by assembling 2032 coin-type cell with monomer or PPPA cathode, Zn plate anode and 2.0 M $Zn(OTf)_2$ aqueous electrolyte, respectively. The CV curve of monomers phenazine and PMDA monomers, and PPPA polymer cathode is shown in Figure S3a, S4a and Figure 2a, respectively. CV profile of the phenazine monomer was featured with one pair of redox peaks centered at about 0.42 and 0.94 V, which is ascribed to one-step two-electron redox reaction for Zn^{2+} storage.[17] By increasing the number of cycles, the CV curves exhibits a continuously shrunk in shape, indicating a decline in capacity, which could be attributed to the serious dissolution problem of phenazine in aqueous electrolyte (Figure S5). On the other hand, the PMDA monomer shows two redox peak couples at 0.66/0.73 V and 0.92/1.03 V, which is respectively originated from the Zn^{2+} and H^+ insertion/extraction process according to the previous reports.[18] After polycondensation reaction to these two monomers, the PPPA polymer only delivers a pair of oxidation/reduction peaks located at around 0.56 and 0.73 V, corresponding to the reversible redox process between carbonyl and enol groups with free radicals. It is noteworthy that the redox peak couples at 0.92/1.03 V for

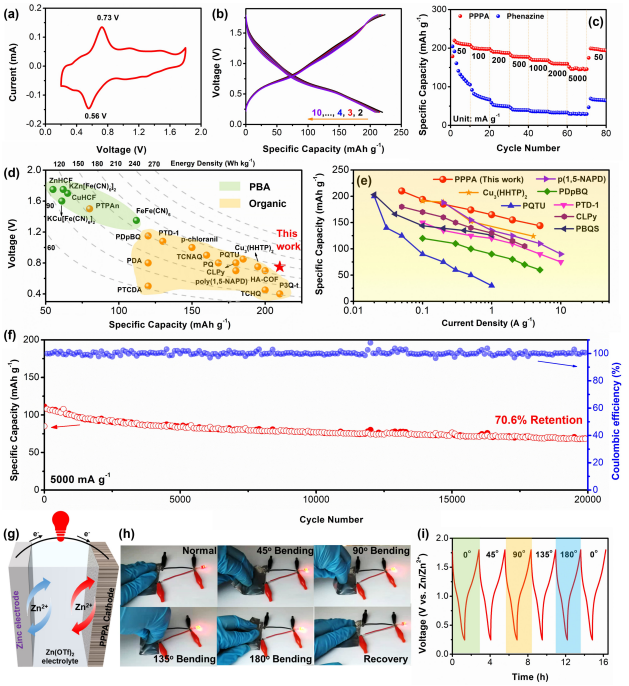

Figure 2. a) CV curves at 0.2 mV s^{-1}. b) GCD curves at 50 mA g^{-1}, and c) rate-performance of PPPA cathode prepared at 24 h. d) Comparison of specific capacities and average discharge voltage between our work and previously reported PBA and organic-based ZIBs.[4a,8,9d,11,18b,19] e) Rate-performance comparison to the state-of-the-art redox polymer cathodes for AZIBs.[10,11,19a–e] f) Long-term cycle performance at 5000 mA g^{-1}. g) Structure illustration of the PPPA-based AZIBs. h) LED indicator lit by a PPPA//Zn pouch cell and i) corresponding GCD curves under various bending state (normal, 45°, 90°, 135°, 180°, and recovery), respectively.

H^+ insertion/extraction process become rather weak after polymerization, suggesting the charge carrier during the electrochemical process is dominated by Zn^{2+} cations rather than protons. In contrast, the as-prepared PPPA at different polymerization time of 2 and 12 h displays similar CV profiles with PPPA polymer prepared at 24 h (Figure S6), which exhibits redox peak couples of 0.57/0.78 V and 0.56/0.76 V, respectively. Such wider voltage gaps suggested their inferior redox reversibility.

The GCD profiles of PPPA cathode is characteristic with slope charge-discharge plateaus and stable capacities around 210 mAh g^{-1} from 2nd to 10th cycle at 50 mA g^{-1} (Figure 2b). Note that the electrochemical stability of PPPA cathode is significantly enhanced compared with that of phenazine and PMDA monomers (Figure S5 and S7). This phenomenon should be originated from that large π-conjugated structure is beneficial to enhance the electrochemical activity and promote the redox reversibility. Figure 2c and Figure S8 depict the rate-performance of a series of PPPA cathodes at various current densities, in which the PPPA cathode prepared at 24 h delivered the best electrochemical performance: a specific capacity of 210.2, 191, 182.1, 170.9, 162.3, 154.4 and 139.7 mAh g^{-1} at a current density of 50, 100, 200, 500, 1000, 2000, and 5000 mA g^{-1} respectively, and also a recovered capacity of 190.6 mAh g^{-1}

when the current density is switched back to 50 mA g^{-1}. As a comparison, phenazine monomer exhibited a poor rate capability with rather small capacity of 72.7, 50.1, 39.4, 35.7, 32.8, and 30 mAh g^{-1} at the current density from 100 to 5000 mA g^{-1}, respectively, and the capacity cannot be returned to its initial value when the current density recovered to 50 mA g^{-1}. This result identifies that zinc-ion storage capacity of quinone compounds can be significantly enhanced via constructing π-conjugated polymer. As depicted in Figure 2d, its energy density surpasses most of conventional cathode counterparts including organics and metal-organic PBAs (based on the mass of active materials in the cathode).[4a,8,9d,11,18b,19] Additionally, our PPPA sample displays superior rate-performance comparable to those of the state-of-the-art redox polymers such as PBQS,[10] PDpBQ,[11] $Cu_3(HHTP)_2$,[19a] PQTU,[19b] poly(1,5-NAPD),[19c] PTD-1,[19d] and CLPy[19e] (Figure 2e). Long-term cycling stability was evaluated at a current density of 5000 mA g^{-1}. The initial capacity was 140.6 mAh g^{-1} and it kept at 92 mAh g^{-1} after 20000 cycles, delivering a capacity retention ratio of 70.6% with coulombic efficiency closing to 100% (Figure 2f). TEM observation of the PPPA cathode before and after 5000 cycles in Figure S9 indicates the PPPA cathode well maintains the initial morphology without drastic structural change after the long-term cycling stability test. We further fabricated a pouch cell constructed by PPPA@carbon fiber cloth flexible cathode, 2.0 M $Zn(OTf)_2$/gelatin-based gel electrolyte and Zn foil anode (Figure 2g). The red LED indicator could be easily lit by the fully charged pouch cell. The brightness remained steady under the varied bending states of 0°, 45°, 90°, 135°, 180°, and recovery (Figure 2h). Furthermore, the corresponding GCD test of the assembled pouch cell under different bending states was shown in Figure 2i with very stable charge-discharge curves. Such an excellent flexibility and folding ability suggests its potential application on flexible, wearable devices.

Known that most of the organic compounds hold Zn^{2+} storage behavior through an ion coordination mechanism.[6–8,11,20a] To clearly unravel the underlying mechanism in our PPPA, electrochemical quartz crystal microbalance (EQCM) measurement was first conducted to in-operando monitor the mass evolution of PPPA cathode during the electrochemical process. Figure 3a depicts the GCD profile of PPPA in one charge/discharge cycle, and there are two slopes respectively at 1.5–0.9 V and 0.7–0.2 V during the discharge process. Analogously, the mass change of PPPA electrode depicts two stages as well, and each stage delivers a similar weight increase of approximately 68 g per mol charge which is well consistent with the hydrated zinc ion ($Zn^{2+}{\cdot}4H_2O$ in average). This result provides evidence that Zn^{2+} cation is the charge carrier when coordinated with the PPPA host, and excludes the possibility of H^+ coordination, the average mass increase of which is usually 18–19 (H_3O^+). This conclusion is further supported by ex situ XRD characterization. Previous study by other groups has revealed that H^+-coordination in quinone during the discharge process is accompanied by the generation of $Zn_m(OTf)_n(OH)_{2m-n}{\cdot}xH_2O$ byproduct.[20a] However, in our

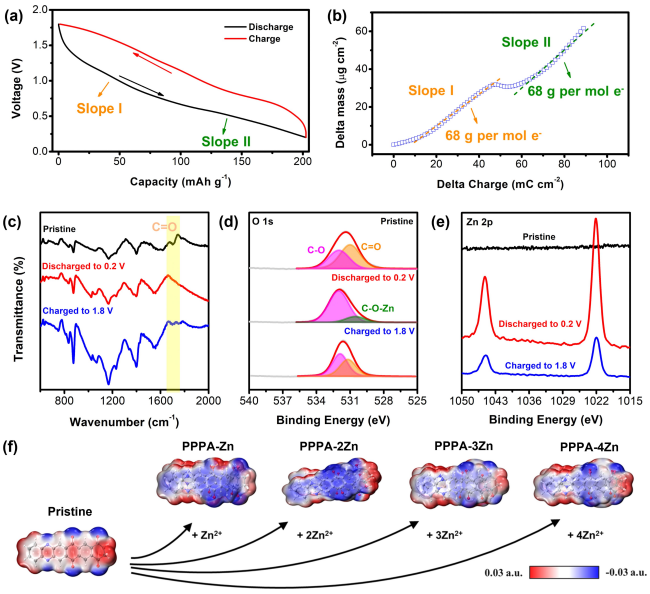

Figure 3. a) GCD profile at 100 mA g^{-1} in QCM measurement. b) Mass change versus charge during the discharge process. Ex situ c) FTIR and d, e) XPS spectra at pristine, fully discharged and charged state, respectively. f) ESP profiles of geometrical configurations during the Zn^{2+}-coordination process.

case, such a byproduct cannot be detected at two typical discharged states of 1.0 and 0.2 V in the ex situ XRD pattern (Figure S10), respectively. SEM-EDS mapping result (Figure S11) further demonstrates that the signal of S element was hardly detected on the surface of the fully discharged cathode at 0.2 V. Moreover, in situ pH measurement was conducted by an operando pH monitor (Figure S12).[20b] It is clearly that the in situ pH profile of the battery cycled with $Zn(OTf)_2$ electrolyte maintains a straight line during the discharging and charging process (Figure S13), further identifying that only Zn^{2+} is the charge carrier in our case and excluding the H^+ involvement.[4a,19a,21]

The charge storage mechanism was further investigated by ex situ FTIR and XPS characterizations. FTIR result in Figure 3c demonstrates that PPPA electrode maintains its initial molecular structure at both fully charged and discharged states. Furthermore, the characteristic peak at 1710 cm^{-1} belonged to carbonyl groups diminished at fully discharged state (0.2 V) and then appeared at the fully charged state (1.8 V), indicating the reversible enolization process of carbonyl groups. XPS characterization further reveals the corresponding bonding changes at pristine, fully discharged, and charged states. In high-resolution O 1s XPS spectrum (Figure 3d), the characteristic peak of C=O group (531 eV) disappeared at the fully discharged state and rose again to a high level at the fully charged state, indicating the reversible conversion between C=O and C–O group in the polymer. Meanwhile, a new C–O–Zn peak (530.5 eV) was detected in the fully discharged state (Figure 3d), which further verifies the Zn^{2+}-coordination with carbonyl groups in the polymer framework during the discharged process.[22] Similar phenomenon was observed in N 1s high-resolution

spectrum (Figure S14), in which the characteristic peak of C=N group (398.9 eV) disappeared at the discharged state and recovered at the charged state. Upon discharging to 0.2 V, the single peak of C–N shifted from 400.2 eV to 399.4 eV, which can be attributed to the increased electron density around the N atoms during the transformation from C=N to C–N.[17] Additionally, Zn 2p XPS spectra in Figure 3e indicates a content rise of Zn species in the sample at the discharged state. Subsequently, it remarkably decreased at the charged state, suggesting the reversible redox reaction between Zn^{2+} and PPPA polymer. The existence of Zn 2p characteristic peaks after fully charge suggests the partial residue of zinc ion in the sample. EDS mapping under TEM observation indicates no apparent changes on C, N, O distribution in the of the pristine, fully discharged, and charged sample (Figure S15). The detection on weak signal of Zn element in the fully charged sample is well consistent with the above-mentioned Zn 2p XPS spectra.

Density functional theory (DFT) calculations were performed to further identify the possible Zn^{2+}-coordination sites in PPPA matrix from the thermodynamics viewpoint (Figure 3f). Electronic static potential (ESP) approach, which is usually employed to deduce the electrophilic or nucleophilic reaction in organic chemistry, has been used to identify the active sites of our PPPA polymer. The ESP distributions of the pristine PPPA polymer in Figure 3f show six regions near the N and O atoms with more negative value, which are regarded as potential active sites with strong chemical affinity to uptake Zn^{2+}. Considering Zn^{2+} cations tend to be coordinated with adjacent electroactive groups due to their divalent state feature, we selected a simplified configuration based on two adjacent PPPA units to simulate the ESP evolution after introducing Zn^{2+} one by one. When one Zn^{2+} cation is introduced, the optimized geometrical configuration (PPPA-Zn) suggests a high electronegativity concentration near the carbonyl groups, which could readily attract more Zn^{2+} cations in the electrolyte to further coordinated with PPPA matrix. This electronegativity enhancement can be maintained when coordination with $2Zn^{2+}$ (PPPA-2Zn). However, the electronegativity around carbonyl groups exhibits a significant decrease and becomes rather weak in the case of PPPA-3Zn, and it should be more difficult to further increase the uptake number of Zn^{2+} at this state. Such a suppose was further supported by the corresponding calculated binding free energies (ΔG) of a suite of different PPPA-nZn configurations (Figure S16). Among them, PPPA-3Zn exhibited lower ΔG of −6.25 eV than that of PPPA-Zn (−2.21 eV), PPPA-2Zn (−4.07 eV), and PPPA-4Zn (−4.93 eV), which indicates an ideal three-step Zn^{2+}-coordination process from PPPA-Zn to PPPA-3Zn. In addition, PPPA-3Zn exhibits the smallest energy gap of 1.38 eV than other configurations (2.38 eV for PPPA-Zn, 1.44 eV for PPPA-2Zn and 1.5 eV for PPPA-4Zn in Figure S17), further confirming this Zn^{2+} coordination configuration processes is the most possible case during the electrochemical process. Although there are six active sites of the pristine PPPA, the theoretical calculation suggests that only three of them can uptake Zn^{2+} ions, resulting in a half of theoretical capacity in the discharge process ($\approx 221\ mAh\,g^{-1}$). This result is well consistent with the experimental value of $210\ mAh\,g^{-1}$ in Figure 2b. Promisingly, this capacity can be further improved by optimizing the molecular structure (Figure S18a). Considering benzene rings in the molecular chain does not contribute any capacity for zinc-ion storage, we prepared an analogue with the removal of benzene rings. This PPPA analogue delivered a capacity of $341.2\ mAh\,g^{-1}$ at $50\ mA\,g^{-1}$, which is 1.5 times higher than that of PPPA precursor (Figure S18b).

The aforementioned DFT simulation on a low energy gap value of 1.38 eV after Zn^{2+} ion coordination suggests fast intramolecular cationic transfer in our PPPA sample. This inspires us to further conduct the galvanostatic intermittent titration technique (GITT) measurement to carefully identify the zinc ion diffusion kinetics (Figure 4a). The Zn^{2+} ion diffusion coefficient could be calculated by the following equation:

$$D = \frac{4}{\pi\tau}\left(\frac{V}{S}\right)^2\left(\frac{\Delta E_s}{\Delta E_t}\right)^2 \quad (1)$$

Where D is diffusion coefficient, τ is relaxation time (20 min in this case), V is the volume of the active material, S is the area of the electrode, ΔE_s and ΔE_t are the voltage change caused by pulse and charge-discharge process, respectively. Surprisingly, we found a very high average Zn^{2+} ion transport coefficient (D_{Zn2+}) of $1.2\times10^{-7}\ cm^2\,s^{-1}$ (Figure 4b). Such a value is several orders of magnitude higher than that of conventional cathode materials including

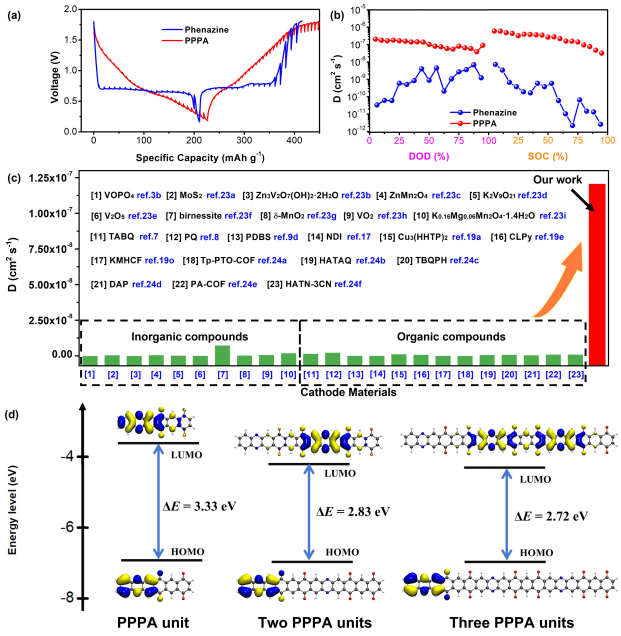

Figure 4. a) GITT curves of PPPA polymer and phenazine monomer during one discharge/charge cycle. b) The corresponding Zn^{2+} ion diffusion coefficient (D) at different depth of discharge (DOD) and state of charge (SOC). c) Comparison of Zn^{2+} diffusion coefficient between PPPA and various inorganic, organic cathodes previously developed. d) HOMO and LUMO energy levels of different PPPA unit configuration by DFT simulation.

metal-organic PBAs,[19o] traditional inorganic cathodes[3b,23] and even the highest one among all the organic cathode materials up to date summarized in Table S2 (Figure 4c and S19).[7,8,9d,17,18a,19a,e,24] We consider such a high D_{Zn2+} should be originated from the intrinsic π-conjugated structure in our PPPA sample, which facilitates the uniform electron delocalization to efficiently enhance the electron transfer on the polymer chains.[11] Moreover, such uniform electron delocalization is beneficial for exposing electronegative sites to the surface of the material for fast capture and coordination of Zn^{2+}.[20] In addition, the electrochemical kinetics were evaluated by CV curves collected at various scan rates from 0.2 to 1.0 $mV s^{-1}$ (Figure S20). As shown in Figure S21a, two pairs of reduction/oxidation peaks for our PPPA cathode are marked as R_1, R_2, O_1, and O_2, respectively. Similarly, the reduction and oxidation peaks of phenazine monomer are marked as R′ and O′, respectively. Generally, the relationship between redox peak current (i) of CV profile and the scan rate (v) can be investigated by the following formula derivation:

$$log(i) = blog(v) + log(a) \quad (2)$$

where a is adjustable parameter and b is the slope. In our case, the b value of R′ and O′ peaks for phenazine monomer are 0.52 and 0.61, respectively, suggesting the charge storage behavior of phenazine is controlled by the ion-diffusion process. Simultaneously, the b value of R_1, R_2, O_1, and O_2 peaks for PPPA cathode are 0.92, 0.98, 0.89, and 0.99 (Figure S21b), respectively, indicating the kinetic behavior of PPPA polymer is mainly controlled by pseudocapacitance effect. Meanwhile, the very analogous b-value between R_1/O_1 (0.92/0.89) and R_2/O_2 (0.98/0.99) redox peaks of our PPPA sample suggests the high redox reversibility, which should be responsible for the high coulomb efficiency closed to 100 % in Figure 2f.[4a] Figure S22 depicts the electrochemical impedance spectroscopy (EIS) measurement of phenazine and our PPPA cathodes. All of the Nyquist plots were consisted of a semicircle in high-frequency region and a sloping line in low frequency region, which was associated with charge-transfer resistance (R_{ct}) and Warburg impedance, respectively. The fitted EIS data identified the R_{ct} of PPPA cathodes is 58.9 Ω, which is much smaller than that of phenazine monomer (185.6 Ω). Consequently, the reaction kinetic is remarkably improved in our PPPA sample after the polymerization.

Finally, we performed DFT calculations to dynamically simulate the growth process of our planar PPPA polymer, which provide more insights on the origin of the ultrafast Zn^{2+} diffusion kinetic. In our case, π-π stacked PPPA polymer was simplified as a linear rigid structure formed by the unidirectional growth of PPPA units, and three typical configurations consisted with one to three units respectively was used to simulate this continuous growth. After geometric optimization, the structural scheme in Figure S23 suggests PPPA polymer molecule well maintains the high molecular planarity with PPPA units increasing one by one during the polymerization process. Such orderly extended structure on the same plane can effectively reduce steric hindrance which generally results in intermolecular sluggish Zn^{2+} diffusion, contributing to the rapid redox reaction dynamics.[4a,11] In addition, the calculation on energy gap between the highest occupied molecular orbital (HOMO) and lowest unoccupied molecular orbital (LUMO) was conducted to evaluate the charge transfer ability of our π-conjugated PPPA polymer. As shown in Figure 4d, the energy gap shows a remarkable decrease with the gradual increase of PPPA unit number (3.33, 2.83, 2.72 eV for one, two and three units respectively). Note that the as-calculated energy gap of 2.72 eV is much smaller than that of the phenazine (3.66 eV)[25] and PMDA (4.7 eV)[26] monomers, and this value would tend to be much smaller with further increasing of PPPA units. Such a great reduce on energy gap could effectively accelerate intramolecular electron transfer during charge/discharge process,[9b,11] giving rise to an ultrahigh Zn^{2+} diffusion coefficient of 1.2×10^{-7} $cm^2 s^{-1}$ as detected by GITT.

Conclusion

In summary, we developed a novel quinone polymer cathode material (PPPA) with typical planar structure by the π-π interaction of polymer chains. When severed as the cathode material for AZIBs, it delivered a high specific capacity of 210.2 $mAh g^{-1}$ at 50 $mA g^{-1}$, and a lifespan over 20000 cycles with 70.6 % capacity retention. EQCM, FTIR and XPS studies verify a reversible Zn^{2+} ion coordination mechanism in our PPPA cathode. Intriguingly, ultrahigh Zn^{2+} ion diffusion coefficient of 1.2×10^{-7} $cm^2 s^{-1}$ was found in this large π-conjugated system. This value is the highest one among all of the organic cathode materials for zinc-ion batteries up to date. DFT calculations reveal the extended π-conjugated plane in our PPPA sample result in a great reduce on energy gap, effectively accelerating intramolecular electron transfer during charge/discharge process. Our study realizes the breakthrough on sluggish Zn^{2+} diffusion kinetics in quinone-based polymer. It also provides insights to achieve high zinc-ion transport kinetics by a design strategy on planar quinone-based polymer system.

Acknowledgements

This work was financially supported by the National Natural Science Foundation of China (Nos. 52171203, 51872051), the Natural Science Foundation of Jiangsu Province (Grants No. BK20211516), the National Key Research and Development Program of China (Grant No. 2021YFB2400400), the State Key Laboratory of New Ceramic and Fine Processing of Tsinghua University (No. KF202102), and the Fundamental Research Funds for the Central Universities (2242022R10090).

Conflict of Interest

The authors declare no conflict of interest.

Data Availability Statement

The data that support the findings of this study are available from the corresponding author upon reasonable request.

Keywords: Energy Gap · Linear Polymer · Organic Zinc-Ion Batteries · Quinone-Based Polymer · Zn^{2+} Diffusion Coefficient

[1] a) Z. D. Huang, Y. Hou, T. R. Wang, Y. W. Zhao, G. J. Liang, X. L. Li, Y. Guo, Q. Yang, Z. Chen, Q. Li, L. T. Ma, J. Fan, C. Y. Zhi, *Nat. Commun.* **2022**, *12*, 4885; b) L. Li, Q. C. Zhang, B. He, R. Pan, Z. X. Wang, M. X. Chen, Z. Wang, K. B. Yin, Y. G. Yao, L. Wei, L. T. Sun, *Adv. Mater.* **2022**, *34*, 2104327; c) H. Zhang, X. Liu, H. H. Li, I. Hasa, S. Passerini, *Angew. Chem. Int. Ed.* **2021**, *60*, 598; *Angew. Chem.* **2021**, *133*, 608; d) G. J. Liang, F. N. Mo, X. L. Ji, C. Y. Zhi, *Nat. Rev. Mater.* **2021**, *6*, 109.

[2] a) P. Chen, T.-T. Li, Y.-B. Yang, G.-R. Li, X.-P. Gao, *Nat. Commun.* **2022**, *13*, 64; b) N. Zhang, X. Y. Chen, M. Yu, Z. Q. Niu, F. Y. Cheng, J. Chen, *Chem. Soc. Rev.* **2020**, *49*, 4203; c) X. X. Jia, C. F. Liu, Z. G. Neale, J. H. Yang, G. Z. Cao, *Chem. Rev.* **2020**, *120*, 7795.

[3] a) Y. X. Zeng, X. F. Lu, S. L. Zhang, D. Y. Luan, S. Li, X. W. (David) Lou, *Angew. Chem. Int. Ed.* **2021**, *60*, 22189; *Angew. Chem.* **2021**, *133*, 22363; b) L. F. Hu, Z. Y. Wu, C. J. Lu, F. Ye, Q. Liu, Z. M. Sun, *Energy Environ. Sci.* **2021**, *14*, 4095; c) J. H. Huang, Z. Wang, M. Y. Hou, X. L. Dong, Y. Liu, Y. G. Wang, Y. Y. Xia, *Nat. Commun.* **2018**, *9*, 2906; d) W. W. Xu, C. L. Sun, K. N. Zhao, X. Cheng, S. Rawal, Y. Xu, Y. Wang, *Energy Storage Mater.* **2019**, *16*, 527.

[4] a) X. L. Wang, J. Tang, W. H. Tang, *Adv. Funct. Mater.* **2022**, *32*, 2200517; b) N. Patil, C. Cruz, D. Ciurduc, A. Mavrandonakis, J. Palma, R. Marcilla, *Adv. Energy Mater.* **2021**, *11*, 2100939.

[5] a) Z. W. Tie, Z. Q. Niu, *Angew. Chem. Int. Ed.* **2020**, *59*, 21293; *Angew. Chem.* **2020**, *132*, 21477; b) T. Sun, J. Xie, W. Guo, D.-S. Li, Q. C. Zhang, *Adv. Energy Mater.* **2020**, *10*, 1904199; c) K. Q. Qin, J. H. Huang, K. Holguin, C. Luo, *Energy Environ. Sci.* **2020**, *13*, 3950.

[6] Q. Zhao, W. W. Huang, Z. Q. Luo, L. J. Liu, Y. Lu, Y. X. Li, L. Li, J. Y. Hu, H. Ma, J. Chen, *Sci. Adv.* **2018**, *4*, eaao1761.

[7] Z. R. Lin, H.-Y. Shi, L. Lin, X. P. Yang, W. L. Wu, X. Q. Sun, *Nat. Commun.* **2021**, *12*, 4424.

[8] B. B. Yang, Y. Y. Ma, D. Bin, H. B. Lu, Y. Y. Xia, *ACS Appl. Mater. Interfaces* **2021**, *13*, 58818.

[9] a) S. B. Zheng, D. J. Shi, D. Yan, Q. R. Wang, T. J. Sun, T. Ma, L. Li, D. He, Z. L. Tao, J. Chen, *Angew. Chem. Int. Ed.* **2022**, *61*, e202117511; *Angew. Chem.* **2022**, *134*, e202117511; b) Y. Zhao, Y. X. Huang, F. Wu, R. J. Chen, L. Li, *Adv. Mater.* **2021**, *33*, 2106469; c) J. Kumankuma-Sarpong, S. Tang, W. Guo, Y. Z. Fu, *ACS Appl. Mater. Interfaces* **2021**, *13*, 4084; d) D. Kundu, P. Oberholzer, C. Glaros, A. Bouzid, E. Tervoort, A. Pasquarello, M. Niederberger, *Chem. Mater.* **2018**, *30*, 3874.

[10] G. Dawut, Y. Lu, L. C. Miao, J. Chen, *Inorg. Chem. Front.* **2018**, *5*, 1391.

[11] X. L. Wang, J. J. Xiao, W. H. Tang, *Adv. Funct. Mater.* **2022**, *32*, 2108225.

[12] Z. P. Song, H. S. Zhou, *Energy Environ. Sci.* **2013**, *6*, 2280.

[13] F. Ye, X. Zhang, K. M. Liao, Q. Lu, X. H. Zou, R. Ran, W. Zhou, Y. J. Zhong, Z. P. Shao, *J. Mater. Chem. A* **2020**, *8*, 9733.

[14] a) Z. W. Tie, L. J. Liu, S. Z. Deng, D. B. Zhao, Z. Q. Niu, *Angew. Chem. Int. Ed.* **2020**, *59*, 4920; *Angew. Chem.* **2020**, *132*, 4950; b) S. Q. Zhang, S. T. Long, H. Li, Q. Xu, *Chem. Eng. J.* **2020**, *400*, 125898.

[15] T. Nokami, T. Matsuo, Y. Inatomi, N. Hojo, T. Tsukagoshi, H. Yoshizawa, A. Shimizu, H. Kuramoto, K. Komae, H. Tsuyama, *J. Am. Chem. Soc.* **2012**, *134*, 19694.

[16] J. Zhang, D. Zhu, M. Matsuo, *Polymer* **2008**, *49*, 5424.

[17] Q. Wang, Y. Liu, P. Chen, *J. Power Sources* **2020**, *468*, 228401.

[18] a) M. Na, Y. Oh, H. R. Byon, *Chem. Mater.* **2020**, *32*, 6990; b) H. Z. Zhang, Y. B. Fang, F. Yang, X. Q. Liu, X. H. Lu, *Energy Environ. Sci.* **2020**, *13*, 2515.

[19] a) K. W. Nam, S. S. Park, R. Reis, V. P. Dravid, H. Kim, C. A. Mirkin, J. Fr Stoddart, *Nat. Commun.* **2019**, *10*, 4948; b) C. X. Guo, Y. Liu, L. Q. Wang, D. J. Kong, J. M. Wang, *ACS Sustainable Chem. Eng.* **2022**, *10*, 213; c) L. Yan, Y. Zhang, Z. G. Ni, Y. Zhang, J. Xu, T. Y. Kong, J. H. Huang, W. Li, J. Ma, Y. G. Wang, *J. Am. Chem. Soc.* **2021**, *143*, 15369; d) G. J. Liang, F. N. Mo, X. L. Ji, C. Y. Zhi, *Angew. Chem. Int. Ed.* **2021**, *60*, 20826; *Angew. Chem.* **2021**, *133*, 20994; e) C. Zhang, W. Y. Ma, C. Z. Han, L.-W. Luo, A. Daniyar, S. H. Xiang, X. Y. Wu, X. L. Ji, J.-X. Jiang, *Energy Environ. Sci.* **2021**, *14*, 462; f) X. J. Yue, H. D. Liu, P. Liu, *Chem. Commun.* **2019**, *55*, 1647; g) Q. Wang, X. Y. Xu, G. Yang, Y. Liu, X. X. Yao, *Chem. Commun.* **2020**, *56*, 11859; h) H. Kobayashi, K. Oizumi, T. Tomai, I. Honma, *ACS Appl. Energy Mater.* **2022**, *5*, 4707; i) W. X. Wang, V. S. Kale, Z. Cao, Y. J. Lei, S. Kandambeth, G. D. Zou, Y. P. Zhu, E. Abouhamad, O. Shekhah, L. Cavallo, M. Eddaoudi, H. N. Alshareef, *Adv. Mater.* **2021**, *33*, 2103617; j) M. S. Chae, S.-T. Hong, *Batteries* **2019**, *5*, 3; k) L. Y. Zhang, L. Chen, X. F. Zhou, Z. P. Liu, *Adv. Energy Mater.* **2015**, *5*, 1400930; l) R. Trócoli, F. L. Mantia, *ChemSusChem* **2015**, *8*, 481; m) M. Görlin, D. O. Ojwang, M.-T. Lee, V. Renman, C.-W. Tai, M. Valvo, *ACS Appl. Mater. Interfaces* **2021**, *13*, 59962; n) Z. Liu, G. Pulletikurthi, F. Endres, *ACS Appl. Mater. Interfaces* **2016**, *8*, 12158; o) T. Cao, F. Zhang, M. J. Chen, T. Shao, Z. Li, Q. J. Xu, D. H. Cheng, H. M. Liu, Y. Y. Xia, *ACS Appl. Mater. Interfaces* **2021**, *13*, 26924.

[20] a) T. Sun, Z.-J. Li, Y.-F. Zhi, Y.-J. Huang, H. J. Fan, Q. C. Zhang, *Adv. Funct. Mater.* **2021**, *31*, 2010049; b) X. S. Xie, H. W. Fu, Y. Fang, B. A. Lu, J. Zhou, S. Q. Liang, *Adv. Energy Mater.* **2022**, *12*, 2102393.

[21] a) M. H. Yu, N. Chandrasekhar, R. K. M. Raghupathy, K. H. Ly, H. Z. Zhang, E. Dmitrieva, C. L. Liang, X. H. Lu, T. D. Kühne, H. Mirhosseini, I. M. Weidinger, X. L. Feng, *J. Am. Chem. Soc.* **2020**, *142*, 19570; b) Z. Y. Song, L. Miao, H. Duan, L. Ruhlmann, Y. K. Lv, D. Z. Zhu, L. C. Li, L. H. Gan, M. X. Liu, *Angew. Chem. Int. Ed.* **2022**, *61*, e202208821; *Angew. Chem.* **2022**, *134*, e202208821.

[22] K. W. Nam, H. Kim, Y. Beldjoudi, T.-W. Kwon, D. J. Kim, J. F. Stoddart, *J. Am. Chem. Soc.* **2020**, *142*, 2541.

[23] a) C. W. Li, C. Liu, Y. Wan, Y. S. Lu, L. Zhu, T. Sun, *Energy Storage Mater.* **2022**, *49*, 144; b) C. Xia, J. Guo, Y. J. Lei, H. F. Liang, C. Zhao, H. N. Alshareef, *Adv. Mater.* **2018**, *30*, 1705580; c) S. Z. Deng, Z. W. Tie, F. Yue, H. M. Cao, M. J. Yao, Z. Q. Niu, *Angew. Chem. Int. Ed.* **2022**, *61*, e2021158; *Angew. Chem.* **2022**, *134*, e2021158; d) B. Y. Tang, G. Z. Fang, J. Zhou, L. B. Wang, Y. P. Lei, C. Wang, T. Q. Lin, Y. Tang, S. Q. Liang, *Nano Energy* **2018**, *51*, 579; e) N. Zhang, Y. Dong, M. Jia, X. Bian, Y. Y. Wang, M. D. Qiu, J. Z. Xu, Y. C. Liu, L. F. Jiao, F. Y. Cheng, *ACS Energy Lett.* **2018**, *3*, 1366; f) G. L. Wang, Y. L. Wang, B. Y. Guan, J. M. Liu, Y. Zhang, X. W. Shi, C. Tang, G. H. Li, Y. B. Li, X. Wang, L. Li, *Small* **2021**, *17*, 2104557; g) H. Tang, W. H. Chen, N. Li, Z. L. Hu, L. Xiao, Y. J. Xie, L. J. Xi, L. Ni, Y. R. Zhu, *Energy Storage Mater.* **2022**, *48*, 335; h) Y. B. Liu, Y. N. Zou, M. Y. Guo, Z. X. Hui, L. J. Zhao, *Chem. Eng. J.* **2022**, *433*, 133528; i) F. Y. Jing, Y. N. Liu, Y. R. Shang, C. D. Lv, L. L. Xu, J. Pei, J. Liu, G. Chen, C. S. Yan, *Energy Storage Mater.* **2022**, *49*, 164.

[24] a) D. X. Ma, H. M. Zhao, F. Cao, H. H. Zhao, J. X. Li, L. Wang, K. Liu, *Chem. Sci.* **2022**, *13*, 2385; b) N. T. H. Luu, A. S.

Ivanov, T.-H. Chen, I. Popovs, J.-C. Leed, W. Kaveevivitchai, *J. Mater. Chem. A* **2022**, *10*, 12371; c) Y. K. An, Y. Liu, S. S. Tan, F. Y. Xiong, X. B. Liao, Q. Y. An, *Electrochim. Acta* **2022**, *404*, 139620; d) J. D. Liang, M. Y. Tang, L. W. Cheng, Q. N. Zhu, R. N. Ji, X. Liu, Q. Zhang, H. Wang, Z. T. Liu, *J. Colloid Interface Sci.* **2022**, *607*, 1262; e) W. X. Wang, V. S. Kale, Z. Cao, S. Kandambeth, W. L. Zhang, J. Ming, P. T. Parvatkar, E. A. -Hamad, O. Shekhah, L. Cavallo, M. Eddaoudi, H. N. Alshareef, *ACS Energy Lett.* **2020**, *5*, 2256; f) Z. L. Ye, S. J. Xie, Z. Y. Cao, L. P. Wang, D. X. Xu, H. Zhang, J. Matz, P. Dong, H. Y. Fang, J. F. Shen, M. X. Ye, *Energy Storage Mater.* **2021**, *37*, 378.

[25] E. Bindewald, R. Lorenz, O. Hübner, D. Brox, D.-P. Herten, E. Kaifera, H.-J. Himmel, *Dalton Trans.* **2015**, *44*, 3467.

[26] Y. Guo, J. C. Yang, S. Chu, F. Kong, L. L. Luo, Y. Wang, Z. G. Zou, *Chem. Phys. Lett.* **2012**, *550*, 175.

Manuscript received: September 27, 2022
Accepted manuscript online: October 26, 2022
Version of record online: November 17, 2022